

Detailed Monte Carlo Simulation of Electron Transport and Electron Energy Loss Spectra

M. ATTARIAN SHANDIZ,¹ F. SALVAT,² AND R. GAUVIN¹

¹Department of Materials Engineering, McGill University, Montreal, Canada

²Facultat de Física (ECM), Universitat de Barcelona, Barcelona, Spain

Summary: A computer program for detailed Monte Carlo simulation of the transport of electrons with kinetic energies in the range between about 0.1 and about 500 keV in bulk materials and in thin solid films is presented. Elastic scattering is described from differential cross sections calculated by the relativistic (Dirac) partial-wave expansion method with different models of the scattering potential. Inelastic interactions are simulated from an optical-data model based on an empirical optical oscillator strength that combines optical functions of the solid with atomic photoelectric data. The generalized oscillator strength is built from the adopted optical oscillator strength by using an extension algorithm derived from Lindhard's dielectric function for a free-electron gas. It is shown that simulated backscattering fractions of electron beams from bulk (semi-infinite) specimens are in good agreement with experimental data for beam energies from 0.1 keV up to about 100 keV. Simulations also yield transmitted and backscattered fractions of electron beams on thin solid films that agree closely with measurements for different film thicknesses and incidence angles. Simulated most probable deflection angles and depth-dose distributions also agree satisfactorily with measurements. Finally, electron energy loss spectra of several elemental solids are simulated and the effects of the beam energy and the foil thickness on the signal to background and signal to

noise ratios are investigated. SCANNING 38:475–491, 2016. © 2015 Wiley Periodicals, Inc.

Key words: electron interactions, Monte Carlo simulations, electron backscattering, electron energy loss spectroscopy

Introduction

The reliability of Monte Carlo (MC) simulation of multiple electron interactions is primarily determined by the accuracy of the adopted differential cross-section (DCS) models. A wide variety of MC models have been used in studies aimed at describing various aspects of the interaction of electron beams with solid specimens, including backscattering, secondary electron emission, x-ray emission and bremsstrahlung photon emission (Joy, '95). The MC programs Casino (Hovington *et al.*, '97) and Win X-ray (Gauvin *et al.*, 2006) were developed by Gauvin and co-workers to simulate electron trajectories in scanning electron microscopy (SEM). In these programs, as well as in other programs used in SEM, electron energy losses are described using the continuous-slowing-down approximation (i.e., by means of the average energy-loss obtained from the Bethe stopping power formula), which is thought to be sufficient when the number of inelastic interactions along each electron trajectory is large. However, for the lower energies (<1 keV) used in SEM and for the high-energy beams in transmission-electron microscopy (TEM), energy straggling is important and one should rely on detailed simulation schemes, where individual inelastic collisions are simulated from the corresponding DCSs. A convenient framework for describing inelastic interactions is provided by the so-called optical-data models (ODM) (Fernández-Varea *et al.*, '93, 2005).

Various MC programs (Shimizu and Ding, '92; Jensen and Walker, '93; Fernández-Varea *et al.*, '96) with detailed simulation of inelastic collisions using different ODMs have been developed. The theoretical

Contract grant sponsor: The National Sciences and Engineering Research Council of Canada (NSERC); Contract grant sponsor: McGill Engineering Doctoral Awards (MEDA) program; Contract grant sponsor: Spanish Ministerio de Economía y Competitividad and ERDF; Contract grant number: project no. FPA2013-44549-P; Contract grant sponsor: Generalitat de Catalunya; Contract grant number: 2014 SGR 846.

Address for reprints: M. Attarian Shandiz, Department of Materials Engineering, McGill University, Montreal, Canada.
E-mail: mohammad.attarianshandiz@mail.mcgill.ca

Received 5 July 2015; Accepted with revision 12 October 2015

DOI: 10.1002/sca.21280

Published online 29 October 2015 in Wiley Online Library
(wileyonlinelibrary.com).

assumptions underlying an ODM are equivalent to the first-order plane-wave Born approximation, in which the DCS is expressed as the product of kinematical factors and the generalized oscillator strength (GOS). The basic ingredient of an ODM is the optical oscillator strength (OOS), that is, the GOS for null momentum transfer. Typically, the OOS is built from optical data (refractive index and extinction coefficient) obtained from experiments or from density functional theory calculations, which are usually available only for relatively small energy transfers, complemented with calculated or experimental photoelectric cross sections for higher energy transfers. While optical data provide a realistic description of low-energy excitations of conduction and valence electrons, photoelectric cross sections usually give the most reliable approximation available for excitations of inner electron shells. The GOS for finite momentum transfers is obtained from the adopted OOS by means of a suitable extension algorithm. In the present work, we follow Fernández-Varea *et al.* ('93), and adopt an extension algorithm that combines an analytical approximation to the one-electron DCS of the free-electron gas, the "two-modes model", for excitations of valence and conduction electrons with the "delta-oscillator model" for excitations of inner shells.

We have developed a generic MC program that performs detailed MC simulations of electrons in a homogeneous specimen of a given thickness. The structure of the program and the adopted sampling methods are similar to those of the program LEEPS (Fernández-Varea *et al.*, '96). However, the considered interactions models are more flexible, and faster and more robust algorithms are used. This program allows the simulation of electron transport in solids of arbitrary composition in a wide range, from about 0.1 keV to about 500 keV.

In the Section Interaction Models, we give an overview of the considered interaction models and sampling methods. The information and models utilized to assemble the OOS of a material are described in the Section Building the OOS. The Section Monte Carlo Simulation gives a brief description of our MC simulation code. Results from simulations of electron backscattering and transmission are compared to available experimental data from various sources in Section Results and Discussions, where we also analyze the effects of the beam energy and the foil thickness on the signal to background and signal to noise ratios in electron-energy-loss (EEL) spectra. Finally some concluding remarks are made in Section Concluding Remarks.

Interaction Models

In the energy range of interest, the dominant interactions of electrons in solids are elastic collisions

and inelastic interactions. Bremsstrahlung emission, which has a continuous energy-loss spectrum and contributes less than $\sim 1.5\%$ to the stopping power of 500 keV electrons, will be disregarded. Elastic collisions may cause relatively large deflections of the electron trajectories, with negligible energy loss. Inelastic interactions induce electronic excitations of the medium, and involve both a loss of energy and a deflection of the projectile electron.

To cover the energy range of interest, we must use relativistic kinematics. We recall that the kinetic energy E and the momentum \mathbf{p} of an electron are related by

$$(cp)^2 = E(E + 2m_e c^2), \quad (1)$$

where m_e is the electron mass and c is the speed of light in vacuum. Moreover,

$$E = (\gamma - 1)m_e c^2 \text{ and } \mathbf{p} = \beta\gamma m_e c \hat{\mathbf{v}} \quad (2)$$

where

$$\beta = \frac{v}{c} = \sqrt{\frac{E(E + 2m_e c^2)}{(E + m_e c^2)^2}} \quad (3)$$

is the velocity v of the electron in units of c , and

$$\gamma = \sqrt{\frac{1}{1 - \beta^2}} = \frac{E + m_e c^2}{m_e c^2} \quad (4)$$

is the total energy in units of the electron rest energy.

Elastic Scattering

Elastic events are characterized by a DCS depending only on the cosine of the polar scattering angle θ , $d\sigma_{el}/d(\cos\theta)$. The DCSs adopted in the simulations were generated by using the computer program ELSEPA (Salvat *et al.*, 2005; Bote *et al.*, 2009). This program computes elastic DCSs by the relativistic (Dirac) partial-wave expansion method, which accounts for spin and relativistic effects in a consistent way (Salvat, 2003). In its default mode, the scattering potential considered in ELSEPA is the sum of the electrostatic potential of the neutral atom (with the electron density obtained from Dirac-Hartree-Fock self-consistent atomic structure calculations) and the local exchange potential of Furness and MacCarthy (Furness and McCarthy, '73). ELSEPA allows slightly more elaborated potential models, which include a polarization term (accounting for the effect of the atomic dipole polarizability) and an absorptive complex potential (which accounts for the depopulation of the elastic channel due to inelastic collisions).

Moreover, the effect of atomic aggregation can be accounted for approximately by using a muffin-tin model potential (Salvat *et al.*, 2005).

The DCSs adopted in the simulations were generated using the ELSEPA default (static plus exchange) potential. In the case of scattering by neutral free atoms, this approach yields DCSs in good agreement with available experimental data for electrons with kinetic energy E higher than about 1 keV (Salvat, 2003, ICRU Report 77, 2007). In the case of compounds and mixtures, the “molecular” DCS is obtained as the incoherent sum of the DCSs of the atoms in a molecule. That is, we disregard aggregation effects and coherent scattering effects, which are expected to be negligible for electrons with energies larger than about 1 keV.

Our simulation program reads a table of DCSs for a dense logarithmic grid of energies E , with 15 points per decade, and a non-uniform grid of 606 polar scattering angles. The DCS for arbitrary energies is calculated by natural cubic spline interpolation, in both E and θ , of the input table. The quantities employed in the simulation of elastic events are the mean free path, λ_{el} , and the probability distribution function, $p(\cos\theta)$, of the angular deflection in each event. The mean free path is given by

$$\lambda_{\text{el}} = \frac{1}{\mathcal{N}\sigma_{\text{el}}}, \quad (5)$$

where \mathcal{N} is the number of molecules per unit volume and

$$\sigma_{\text{el}} = \int_{-1}^1 \frac{d\sigma_{\text{el}}}{d\cos\theta} d(\cos\theta) \quad (6)$$

is the total elastic cross section. The angular distribution is

$$p_{\text{el}}(\cos\theta) = \frac{1}{\sigma_{\text{el}}} \frac{d\sigma_{\text{el}}}{d\cos\theta} \quad (7)$$

The random sampling of $\cos(\theta)$ is performed by using the RITA algorithm (rational inverse transform with aliasing, see Ref. (Salvat *et al.*, 2011), which combines an adaptive rational interpolation of the inverse cumulative function with Walker’s aliasing method. This sampling algorithm is extremely fast and accurate; interpolation errors are less than about 10^{-4} , and are usually masked by statistical uncertainties. An initialization routine precalculates tables of sampling parameters for a dense logarithmic grid of energies E_i , which are stored in memory. In principle, the angular distribution at the current energy E is obtained by linear interpolation in $\ln(E)$. That is, if $E_i \leq e \leq E_{i+1}$, we set

$$p_{\text{el}}(E; \cos\theta) = \pi_i p_{\text{el}}(E_i; \cos\theta) + \pi_{i+1} p_{\text{el}}(E_{i+1}; \cos\theta) \quad (8a)$$

with

$$\begin{aligned} \pi_i &= \frac{\ln E_{i+1} - \ln E}{\ln E_{i+1} - \ln E_i} \quad \text{and} \\ \pi_{i+1} &= \frac{\ln E - \ln E_i}{\ln E_{i+1} - \ln E_i}. \end{aligned} \quad (8b)$$

However, there is no need of actually performing the interpolation, because we can sample $\cos(\theta)$ only for the energies E_i of the grid. The trick is to regard the interpolated distribution as an statistical mixture of the distributions at E_i and E_{i+1} , with interpolation weights π_i and π_{i+1} , which are positive and add to unity. Consequently, the random sampling of $\cos(\theta)$ can be performed by using the composition method, as follows: (1) sample a random index k , which can take the values i or $i+1$ with point probabilities π_i and π_{i+1} , and (2) sample $\cos(\theta)$ from the distribution $p_{\text{el}}(E_k; \cos\theta)$ by using the RITA algorithm.

Inelastic Scattering

As inelastic interactions play a central role in the determination of EEL spectra, the DCSs utilized in the simulations will be presented in some detail. For electrons with kinetic energy less than about 500 keV we can use a semi-relativistic form of the plane-wave (first) Born approximation (Fernández-Varea *et al.*, ’96). Since we are mostly interested on the effect of inelastic interactions on the projectile, we consider the doubly-differential cross section (DDCS) depending on the energy transfer W and the polar scattering angle θ . Each interaction alters the energy E and the momentum \mathbf{p} of the projectile; the corresponding values after the interaction are

$$E' = E - W \quad \text{and} \quad \mathbf{p}' = \mathbf{p} - \mathbf{q}, \quad (9)$$

where \mathbf{q} is the momentum transfer. Note that

$$p' = c^{-1} \sqrt{(E - W)(E - W + 2m_e c^2)} \quad (10)$$

and

$$q^2 = p^2 + p'^2 - 2pp' \cos\theta. \quad (11)$$

Instead of the scattering angle, it is more convenient to express the DDCS in terms of the recoil energy Q defined by (Fano, ’63; Fernández-Varea *et al.*, 2005)

$$Q(Q + 2m_e c^2) = (cq)^2. \quad (12)$$

The DDCS derived from the Born approximation can be expressed as (Inokuti, ’71)

$$\frac{d\sigma_{\text{in}}^2}{dQ dW} = \frac{2\pi e^4}{m_e v^2} \frac{1}{WQ} \frac{df(Q, W)}{dW}, \quad (13)$$

where e is the electron charge, v is the velocity of the projectile, and $df(Q, W)/dW$ is the generalized oscillator strength (GOS). This DCS has the form of the non-relativistic DCS (Inokuti, '71); the main relativistic effects are accounted for through the use of the relativistic velocity, $v = \beta c$ in Eq. (13), and of relativistic kinematics. It should be noted that Eq. (13) accounts only for the instantaneous Coulomb interaction, the so-called longitudinal interaction. We are disregarding the contribution from the transverse interactions (exchange of virtual photons between the projectile and the electrons in the medium), which has a small effect for electrons with energies less than about 500 keV, and can be neglected for the purposes of the present study.

In the optical limit ($Q \rightarrow 0$), the GOS reduces to the optical oscillator strength (OOS), $df(W)/dW$, which is proportional to the photoelectric cross section of photons of energy W , calculated within the dipole approximation,

$$\frac{df(W)}{dW} \equiv \frac{df(Q, W)}{dW} = \frac{m_e c}{2\pi^2 e^2 \hbar} \sigma_{\text{ph}}(W). \quad (14)$$

The GOS satisfies the Bethe sum rule (Inokuti, '71)

$$\int_0^\infty \frac{df(Q, W)}{dW} dW = Z_m \quad \forall Q, \quad (15)$$

where Z_m is the total number of electrons in a molecule.

For a given energy loss W , the allowed values of the recoil energy lie in the interval (Q_-, Q_+) , with endpoints given by Eq. (11) and (12) with $\cos\theta = +1$ and -1 , respectively. That is,

$$Q_{\pm} = \sqrt{[c(p \pm p')]^2 + m_e^2 c^4} - m_e c^2. \quad (16)$$

When $W \ll E$, the lowest allowed recoil energy can be calculated from the approximate relation (see, e.g., Ref. (Fernández-Varea *et al.*, 2005))

$$Q_- (Q_- + 2m_e c^2) = W^2 / \beta^2 \quad (17)$$

The precise value of Q_+ , which is always larger than W , is quite irrelevant, because the GOS vanishes for $Q \gtrsim W$. The energy-loss DCS is obtained by integrating over the kinematically allowed values of the recoil energy,

$$\frac{d\sigma_{\text{in}}}{dW} \equiv \int_{Q_-}^{Q_+} \frac{d^2\sigma_{\text{in}}}{dW dQ} dQ, \quad (18)$$

The mean free path λ_{in} in for inelastic collisions is

$$\lambda_{\text{in}} = \frac{1}{\mathcal{N} \sigma_{\text{in}}}, \quad (19)$$

where \mathcal{N} is the number of atoms or molecules per unit volume, and

$$\sigma_{\text{in}} = \int_0^{W_{\text{max}}} \frac{d\sigma_{\text{in}}}{dW} dW \quad (20)$$

is the total cross section for inelastic interactions. The quantity W_{max} is the maximum energy loss in an interaction which, considering the projectile and the active target electron as distinguishable, is equal to E . The stopping power, i.e. the average energy loss per unit volume, is given by

$$S_{\text{in}} = \mathcal{N} \int_0^{W_{\text{max}}} W \frac{d\sigma_{\text{in}}}{dW} dW, \quad (21)$$

where the integral defines the stopping cross section.

Alternatively, the slowing down of electrons caused by inelastic interactions can be described by using the semi-classical dielectric formalism (Lindhard, '54; Fano, '63; Fernández-Varea *et al.*, 2005), that is, by considering the specimen as an isotropic dielectric material and by assuming a linear response to external electromagnetic fields. Under these assumptions, the medium is characterized by a complex dielectric function $\epsilon(k, \omega)$, which depends on the angular frequency ω and the wavenumber k of electromagnetic disturbances. The passage of fast charged particle originates an induced electromagnetic field which exerts a stopping force on the projectile. The explicit calculation of this force (see, e.g., Ref. (Lindhard, '54)) leads to an expression that is strictly equivalent to the right-hand side of Eq. (21) if one makes the identification

$$\frac{df(Q, W)}{dW} \equiv W (1 + Q/m_e c^2) \frac{2Z}{\pi \Omega_p^2} \text{Im} \left(\frac{-1}{\epsilon(k, \omega)} \right). \quad (22)$$

where $\epsilon(k, \omega)$ is the value of the dielectric function at $k = q/\hbar$ and $\omega = W/\hbar$, and Ω_p is the plasma resonance energy of a homogeneous free-electron gas with the electron density of the medium,

$$\Omega_p = \sqrt{4\pi \mathcal{N} Z_m \hbar^2 e^2 / m_e}. \quad (23)$$

Note that the OOS and the optical dielectric function, $\epsilon(\omega) \equiv \epsilon(0, \omega)$, are related by

$$\frac{df(W)}{dW} \equiv W \frac{2Z}{\pi\Omega_p^2} \text{Im} \left(\frac{-1}{\epsilon(\omega)} \right). \quad (24)$$

The optical dielectric function determines the refractive index $n(\omega)$ and the extinction coefficient $k(\omega)$ of the material, which are defined by the equality $n(\omega) + ik(\omega) = \sqrt{\epsilon(\omega)}$, where the branch of the square root is the one yielding a non-negative n .

The GOS can be expressed as the sum of contributions from the various atomic electron subshells. Subshells with binding energy larger than about 75 eV are considered as inner subshells. As the orbitals of these subshells are only weakly affected by the presence of neighboring atoms, their GOSs can be approximated by those of free atoms calculated, e.g. by using self-consistent Dirac-Hartree-Fock-Slater atomic electron orbitals (Bote and Salvat, 2008). However, the calculation of GOS of outer subshells, with smaller binding energy, and of valence and conduction electrons is not always possible with current theoretical and computational methods, and one must rely on approximate semi-empirical models. The most elaborate GOSs available are provided by the so-called optical-data models, in which the GOS is constructed from an experimental, semi-empirical or calculated OOS, from which the GOS for $Q > 0$ is generated by means of physically motivated extension algorithms, usually based on the response of a free-electron gas (FEG). Our procedure for building OOS is described in detail in Section Building the OOS below.

To set a plausible extension algorithm, it is convenient to consider the GOS of a FEG, as obtained from Lindhard's dielectric function. This dielectric function is given by a closed analytical expression, and accounts for both plasmon and electron-hole excitations. The resulting GOS, however, it is too complicated for simulation purposes. To ease the calculations, Fernández-Varea *et al.* ('93) proposed the following simple approximation to the GOS per electron of a FEG,

$$F_{\text{TM}}(W_p; Q, W) = \left(1 - f_p(Q)\right) \delta(W - W_r(Q)) + f_p(Q) \delta(W - Q), \quad (25a)$$

where W_p is the plasma-resonance energy of the FEG, $\delta(x)$ is the Dirac delta distribution,

$$f_p(Q) = \min \left\{ 1, \frac{AQ^3}{W_p^2(W_p + Q)} \right\}, \quad (25b)$$

$$W_r(Q) = W_p + BQ,$$

and the parameters A and B are given by

$$A = \begin{cases} 2/3, & \text{if } \omega \leq 0.62 \text{ eV}, \\ 0.9069 + 0.3577\omega^2 - 1.565\omega^3 + 1.478\omega^4 - 0.4524\omega^5, & \text{if } \omega > 0.62 \text{ eV}, \end{cases} \quad (25c)$$

and

$$B = 0.2598 + (0.3532/\omega) \quad (25d)$$

with $\omega = (W/\text{eV})^{-1/3}$. In spite of its simplicity, this approximation keeps the essential physics of Lindhard's theory. The two terms (modes) in expression (25a) describe, respectively, plasmon excitation and electron-hole excitations. The plasmon line is defined by the dispersion relation $W = W_r(Q)$, which agrees closely with Lindhard's theory at small Q , and electron-hole excitations are localized on the line $W = Q$ of the (Q, W) plane (Bethe ridge), which corresponds to binary collisions with free electrons at rest. While plasmon excitation occurs only for recoil energies less than a cutoff value Q_c (the lowest Q for which $f_p(Q) = 0$), electron-hole excitations are possible for arbitrary energy transfers, from 0 to E . The main difference between the approximation (Eq. (25a)) and the actual (Lindhard) GOS of the FEG is the neglect of the finite width of Lindhard's electron-hole continuum, i.e. the Bethe ridge is collapsed into a zero-width resonance. The parameters A and B were determined so as to ensure that the inelastic mean free path and the stopping power calculated from the GOS (Eq. (25)) practically coincide with those obtained from the Lindhard dielectric function (Fernández-Varea *et al.*, '93).

Evidently, the GOS (Eq. (25)) satisfies the Bethe sum rule (for one target electron),

$$\int_0^\infty F_{\text{TM}}(W_p; Q, W) dW = 1 \quad \forall Q, \quad (26)$$

and reduces to the form $\delta(W - W_p)$ of a sharp resonance at $Q = 0$. Our optical-data model utilizes the "two-modes model" (Eq. (25a)) as extension algorithm for excitations of valence and conduction electrons. That is, the GOS for these excitations is approximated in the form

$$\frac{df(Q, W)}{dW} = \int_0^\infty \left[\frac{df(W')}{dW'} \right]_{\text{exp}} F_{\text{TM}}(W'; Q, W) dW', \quad (27)$$

where $[df(W)/dW]_{\text{exp}}$ is the experimental OOS. That is, the GOS is expressed as an admixture of FEGs of different plasma energies, weighted so as to reproduce the experimental OOS. Evidently, this GOS reduces to the adopted OOS at $Q = 0$.

The two-modes model (as well as the “exact” Lindhard GOS of the FEG) is not appropriate for modeling excitations of electrons in inner subshells. The reason is that ionization of an inner subshell occurs only when the energy transfer is larger than the corresponding binding energy, whereas the two-modes model allows arbitrarily small energy transfers. Following Fernández-Varea *et al.* ('96), for inner-shell excitations we use a simpler extension algorithm, the so-called delta oscillator, defined by

$$F_{\delta}(W'; Q, W) \equiv \delta(W - W')\Theta(W' - Q) + \delta(W - Q)\Theta(Q - W'), \quad (28)$$

where $\Theta(x)$ is the unit step function ($=1$ if $x < 0$, $=0$ otherwise). The two terms in this expression represent resonant distant interactions and binary close collisions, respectively. Note that the delta oscillator only allows energy transfers larger than the resonance energy, and satisfies the one-electron sum rule (Eq. (26)).

Because we normally do not have the OOS decomposed into contributions from different inner subshells and bands, we shall use the two-modes model for W' less than a fixed switch energy W_s , and the delta oscillator for resonance energies above W_s . In the calculations we take the switch energy equal to the lowest ionization energy of electron subshells which is larger than about 75 eV, because low- Q excitations with $W \lesssim W_s$ do have a small- Q component with plasmon-like (collective) character. That is, we set

$$\frac{df(Q, W)}{dW} = \int_0^{W_s} \left[\frac{df(W')}{dW'} \right]_{\text{exp}} F_{\text{TM}}(W'; Q, W) dW' + \int_{W_s}^{\infty} \left[\frac{df(W')}{dW'} \right]_{\text{exp}} F_{\delta}(W'; Q, W) dW' \quad (29)$$

Evidently, if the OOS satisfies the Thomas-Reiche-Kuhn sum rule

$$\int_0^{\infty} \left[\frac{df(W)}{dW} \right]_{\text{exp}} dW = Z_m, \quad (30)$$

the Bethe sum rule (Eq. (15)) is automatically satisfied.

It is convenient to write the DDCS in the form

$$\frac{d\sigma_{\text{in}}^2}{dQ dW} = \int_0^{\infty} \left[\frac{df(W')}{dW'} \right]_{\text{exp}} \frac{d\sigma^2(W')}{dQ dW} dW' \quad (31)$$

with

$$\frac{d\sigma^2(W')}{dQ dW} = \frac{2\pi e^4}{m_e v^2} \frac{1}{WQ} F_{\text{TM},\delta}(W'; Q, W). \quad (32)$$

The latter quantity can be regarded as the DDCS for excitation of a “one-electron oscillator” with resonance energy W' , represented by the GOS of either the two-modes model or the delta-oscillator, as prescribed by the adopted switch energy.

The plane-wave Born approximation does not account for exchange effects, which result from the indistinguishability of the projectile and the active target electron in the material. For low- Q excitations, these effects can be described by means of the modified Ochkur approximation (Ochkur, '65; Fernández-Varea *et al.*, '93), which introduces a simple factor into the DDCS. The corrected DDCS for excitations of a one-electron oscillator with resonance energy E

$$\frac{d\sigma^2(W')}{dQ dW} = \frac{2\pi e^4}{m_e v^2} \frac{1}{WQ(1 + Q/2m_e c^2)} C_{\text{ex}} F_{\text{TM},\delta}(W'; Q, W) \quad (33)$$

with

$$C_{\text{ex}} = 1 + \left(\frac{Q}{E + D - W} \right)^2 - \frac{Q}{E + D - W} \quad (34)$$

where the first term accounts for direct interactions, the second term represents exchange collisions (in which the projectile and target electrons exchange places) and the third term results from interference of the wave functions of the two emerging electrons. The prescription (Eq. (34)) differs from the original Ochkur correction by the presence of the energy D , which is interpreted as the effective binding energy of the target electron in its initial state. This energy is set equal to the resonance energy W' for delta oscillators, and equal to zero for the two-modes model because conduction and valence electrons have null or small binding energies.

We apply the Ochkur correction only to interactions with Q smaller than the onset of the Bethe ridge. These are, in the case of the two-modes model, electron-hole interactions with Q less than the plasmon cutoff Q_c , and, in the case of the delta oscillator, resonant distant interactions. For plasmon excitation, we set $C_{\text{ex}} = 1$, because these interactions do not involve the ejection of a secondary electron. Interactions on the Bethe ridge are represented as binary collisions with free electrons at rest. The “exact” energy-loss DCS (within the plane-wave Born approximation, and including transverse interactions) for these collisions is given by the modified Moller formula (Moller, '32; Fernández-Varea *et al.*, 2005),

$$\frac{d\sigma_{\text{M}}}{dW} = \frac{2\pi e^4}{m_e v^2} \frac{1}{W^2} \left[1 + \left(\frac{W}{E + D - W} \right)^2 - \frac{(1-a)W}{E + D - W} + \frac{aW^2}{(E + D)^2} \right] \quad (35a)$$

where

$$a = \left(\frac{E}{E + m_e c^2} \right)^2. \quad (35b)$$

We set $D = W'$ for delta oscillators and $D = 0$ for the two-modes model. Accordingly, the exchange factor for interactions on the Bethe ridge is

$$C_{\text{ex}} = 1 + \left(\frac{W}{E + D - W} \right)^2 - \frac{(1-a)W}{E + D - W} + \frac{aW^2}{(E + D)^2}. \quad (35c)$$

The introduction of the exchange correction requires the redefinition of the maximum allowed energy loss W_{max} . Because of the indistinguishability of the projectile and the struck electron after the collision, we are free to consider the “primary” electron as being the fastest of the two. Since they have kinetic energies $E - W$ and $W - D$, the maximum allowed energy loss occurs in the situation where the final energies of the two electrons are equal. That is,

$$W_{\text{max}} = \frac{1}{2}(E + D). \quad (36)$$

It should be noted that this does not imply neglecting interactions with larger energy transfers (where the “projectile” emerges with less energy than the struck electron), because these interactions are represented by the second terms in expressions (34) and (35c); the final terms arise from interference between the wave functions of the two electrons and from relativistic corrections.

The advantage of using simple extension algorithms is that most of the calculations, including the random sampling of W and $\cos(\theta)$ in inelastic interactions, can be performed easily. Details of the numerical calculations and sampling methods are given by Ref. (Fernández-Varea *et al.*, 2005), and references therein. The simulation is simplified by considering the resonance energy of the active oscillator, W' , as a random variable with the following probability distribution function,

$$p_{\text{in}}(W') = \left[\frac{df(W')}{dW'} \right]_{\text{exp}} \frac{\sigma_{\text{TM},\delta}(W')}{\sigma_{\text{in}}}, \quad (37)$$

where

$$\sigma_{\text{TM},\delta}(W') = \int_0^{W_{\text{max}}} dW \int_{Q_-}^{Q_+} dQ \frac{d\sigma^2(W')}{dQ dW}, \quad (38)$$

is the total cross section for excitations of the active oscillator. In our simulation program the cumulative distribution of W'

$$\mathcal{P}(E; W') \equiv \int_0^{W'} p_{\text{in}}(W'') dW'', \quad (39)$$

is precalculated for a dense grid of energies E_i and stored in memory. The cumulative distribution for a given energy is defined by linear interpolation in $\ln(E)$,

$$\mathcal{P}_{\text{in}}(E; W') = \pi_i \mathcal{P}_{\text{in}}(E_i; W') + \pi_{i+1} \mathcal{P}_{\text{in}}(E_{i+1}; W'). \quad (40)$$

With the aid of the interpolation by weight method [cf. Eq. (8)], W' is effectively sampled only for the energies E_i in the grid, by using the inverse transform method. Finally, the values of W and Q are sampled from the (normalized) DDOS of the active oscillator using analytical formulas.

The polar deflection of the projectile is given by Eqs. (11) and (12),

$$\cos\theta = \frac{(cp)^2 + (cp')^2 - Q(Q + 2m_e c^2)}{2c^2 pp'}. \quad (41)$$

Inelastic interactions may result in the emission of secondary electrons. The initial energy of a secondary electron is equal to $E - E_B$, where E_B is the binding energy of the target electron in its initial level (0 for conduction electrons). Because a partition of the OOS into contributions from the various subshells is not generally available, we replace E_B by the effective binding energy D of the active oscillator, which is set equal to 0 for the two-modes model and equal to the resonance energy W' for delta oscillators. When the energy transfer is larger than D , we consider that a secondary electron is released with kinetic energy $W - D$. The polar angle of the initial direction of the secondary electron, θ_r , is set equal to that of the momentum transfer \mathbf{q} . Squaring the identity $\mathbf{p}' = \mathbf{p} - \mathbf{q}$ we obtain

$$\begin{aligned} \cos\theta_r &= \frac{p^2 + q^2 - p'^2}{2pq} \\ &= \frac{E(E + 2m_e c^2) + Q(Q + 2m_e c^2) - (E - W)(E - W + 2m_e c^2)}{2\sqrt{E(E + 2m_e c^2)Q(Q + 2m_e c^2)}} \end{aligned} \quad (42)$$

Building the OOS

Traditionally, the OOSs employed in optical-data models were obtained by combining available experimental optical information (refractive index, extinction coefficient) on the material with inner-shell photoelectric cross sections of free atoms. The most authoritative source of measured optical information are the three volumes of the Handbook of Optical Constants of Solids (Palik, '85, '91, '98), which provide optical dielectric functions for photon energies in the long-

wavelength range, up to some keV, for metals, semiconductors and insulators. Subshell photoelectric cross sections, calculated from the independent-electron approximation, with the Dirac-Hartree-Fock-Slater self-consistent potentials, are available from various databases and publications (Scofield, '73; Cullen *et al.*, '97; Berger *et al.*, 2005; Salvat *et al.*, 2011). The OOSs of the materials Be, Al, Si, Cu, and Au employed in the present simulations were generated in this way.

While for energy transfers larger than about 100 eV, the OOS can be reasonable approximated from X-ray photoelectric data, experimental optical information available for lower energy transfers is quite scarce and for a limited number of materials. Moreover, experimental OOSs are typically inferred from a variety of measured data, acquired from different specimens, using different techniques and instruments, and affected by different sources of uncertainty (see, e.g., Palik, '85). When accurate optical functions are not available, dielectric functions can be calculated numerically with modern density functional theory codes. Additionally, OOSs can be derived from electron energy-loss measurements.

OOS From Density-Functional Theory

The OOS of simple solids between the infrared and soft X-ray frequencies can be calculated by using the method described by Werner *et al.* (2009). The program OPTIC of Ambrosch-Draxl and Sofo (Ambrosch-Draxl and Sofo, 2006) calculates dielectric functions within the random-phase approximation from electronic wave functions computed by the WIEN2k code (Blaha *et al.*, 2001; Schwarz and Blaha, 2003), which solves the Kohn-Sham equations by using the linearized augmented plane-wave method. We have used this approach to compute the low-energy OOS of P and NiO employed in our simulations. In the WIEN2k calculations for P we used the exchange-correlation potential given by the generalized gradient approximation of Perdew *et al.* ('96). In the case of NiO, which exhibits a strongly correlated behavior (Koller *et al.*, 2011), we used the modified Becke-Johnson exchange potential (Becke and Johnson, 2006; Koller *et al.*, 2011) and local density approximation as the correlation potential. Modified Becke-Johnson exchange potential provides a more accurate description of the band gap in semiconductors and strongly correlated systems (Koller *et al.*, 2011).

OOS From EEL Spectra

The OOS can also be inferred from EEL spectra measurements on thin specimens where single-

scattering prevails, i.e. specimens with thickness t much smaller than the mean free path λ_{in} which, for energies higher than 100 keV, is larger than about 100 nm (see, e.g., Fernández-Varea *et al.*, 2005). The collected spectrum corresponds to electrons that have undergone inelastic interactions with scattering angle less than the effective collection semi-angle θ_{max} of the experimental setup. Typically, θ_{max} is small (a few degrees) and the initial kinetic energy is much larger than the observed energy losses. Under these circumstances ($\theta_{max} \ll 1$, $W \ll E$), the relevant interactions involve small recoil energies ($Q \ll 2m_e c^2$) in the interval between the kinematical minimum (for $\theta = 0$),

$$Q_- \simeq \frac{(p - p')^2}{2m_e}, \quad (43)$$

and the value $Q(\theta_{max})$ corresponding to the maximum deflection of the detected electrons,

$$\begin{aligned} Q(\theta_{max}) &\simeq \frac{(p - p')^2}{2m_e} + \frac{pp'}{m_e} (1 - \cos\theta_{max}) \\ &\simeq Q_- + \frac{E(E + 2m_e c^2)}{m_e c^2} 2\sin^2(\theta_{max}/2). \end{aligned} \quad (44)$$

The measured energy-loss spectrum is then given by

$$I(W) = I_0 \varepsilon_d t \mathcal{N} \left[\frac{d\sigma}{dW} \right]_{\theta < \theta_{max}}, \quad (45)$$

where I_0 is the number of incident electrons, ε_d is the efficiency of the detector, and the last factor is the restricted energy-loss DCS,

$$\begin{aligned} \left[\frac{d\sigma}{dW} \right]_{\theta < \theta_{max}} &= \int_{Q_-}^{Q(\theta_{max})} \frac{d^2\sigma}{dQ dW} dQ \\ &\simeq \frac{2\pi e^4}{m_e v^2} \frac{1}{W} \frac{df(W)}{dW} \ln \left[\frac{Q(\theta_{max})}{Q_-} \right]. \end{aligned}$$

Introducing the approximation [see Eq. (17)],

$$Q_- \simeq \frac{W^2}{2m_e c^2 \beta^2},$$

we have

$$\begin{aligned} \left[\frac{d\sigma}{dW} \right]_{\theta < \theta_{max}} &\simeq \frac{2\pi e^4}{m_e v^2} \frac{1}{W} \frac{df(W)}{dW} \\ &\ln \left[1 + \left(\frac{E + 2m_e c^2}{E + m_e c^2} \frac{2E}{W} \right)^2 \sin^2(\theta_{max}/2) \right], \end{aligned} \quad (46)$$

This result shows explicitly that the small-angle energy spectrum is determined primarily by the OOS,

i.e. it is essentially independent of the adopted extension algorithms. The OOS can thus be derived from the EEL spectrum, except possibly an instrumental constant which may eventually be obtained by invoking the Bethe sum rule.

Monte Carlo Simulation

The input information for simulation in a given material reduces to the table of elastic DCSs generated by ELSEPA and a table of values of the OOS covering the relevant range of excitation energies. The energies of the OOS table are sufficiently spaced to ensure that log-log linear interpolation of the OOS does not introduce any significant distortions. The OOS used in our simulations were built by combining experimental optical data or results from density functional theory calculations with X-ray photoelectric data. The only additional parameter is the switch energy, (W_s), which determines the interval where each extension algorithm (two-modes model or delta oscillator) applies.

The generation of random electron trajectories is performed by the conventional detailed (event by event) simulation method. The DCSs, and other relevant quantities derived from them, depend on the kinetic energy E of the transported electron. The total cross section is

$$\sigma_T = \sigma_{el} + \sigma_{in}, \quad (47)$$

The total mean free path, defined by

$$\lambda_T = (\mathcal{N}\sigma_T)^{-1}, \quad (48)$$

gives the interaction probability per unit path length. The probability density of the path length s to the next interaction is

$$p(s) = \frac{1}{\lambda_T} \exp(-s/\lambda_T). \quad (49)$$

Consider an electron starting its motion from a point \mathbf{r} with energy E and direction specified by the unit vector $\hat{\mathbf{d}}$. The length s of the free flight to the next interaction is generated using the sampling formula

$$s = -\lambda_T \ln(\xi), \quad (50)$$

where ξ is a random number uniformly distributed between 0 and 1. The electron is moved to its new position, $\mathbf{r} + s\hat{\mathbf{d}}$. The kind of interaction, elastic or inelastic, that occurs there is selected randomly according to the respective point probabilities, $p_{el} = \sigma_{el}/\sigma_T$ and $p_{in} = \sigma_{in}/\sigma_T$. If the interaction is elastic, the

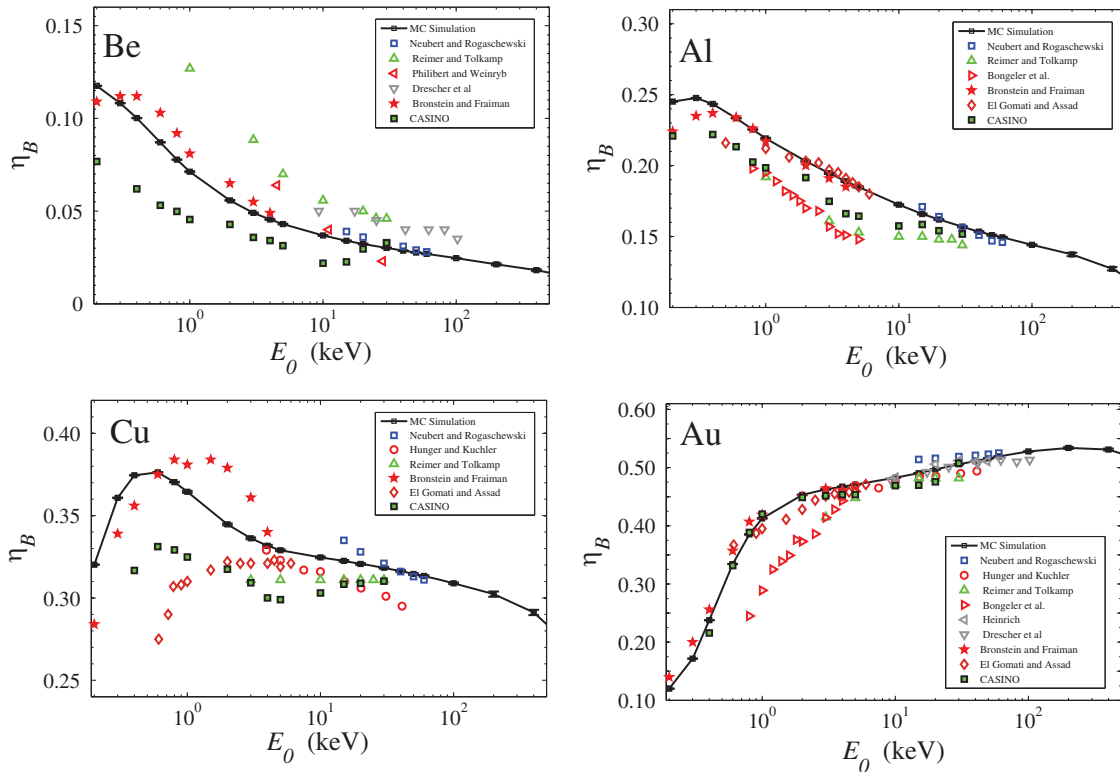


Fig 1. Backscattering coefficient η_B of electron beams impinging normally on thick specimens of Be, Al, Cu, and Au, as a function of the beam energy. Dashed lines represent results from present MC simulations; symbols are experimental data from the database compiled by Joy (2008), and simulation results from the CASINO program.

polar deflection $\cos\theta$ is sampled from the probability distribution (Eq. (7)) using the numerical algorithms described in Section Elastic Scattering. If the interaction is inelastic, random values of the energy loss W and the angular deflection $\cos\theta$ are generated by using the strategy sketched in Section Inelastic Scattering. In both cases, the azimuthal scattering angle ϕ is sampled uniformly in the interval $(0, 2\pi)$. The values $\cos\theta$ and ϕ determine the direction \hat{d} of the electron after the interaction. In inelastic events the energy of the electron is reduced and, when a secondary electron is released, its initial position, direction and energy are stored in memory. The simulation proceeds by iterating these operations, until the electron leaves the specimen or its energy becomes smaller than a selected absorption (cutoff) energy. After completing the trajectory of an electron, the program loads the last electron in the secondary stack and tracks it. The simulation of the shower induced by a primary electron ends when the stack is empty.

Results and Discussions

The simulation results presented below were generated from independent runs of our MC code. Transported electrons were assumed to be absorbed in the material when their kinetic energy became less than 50 eV. The number of simulated electron showers in each run was larger than 1 million, so that the statistical uncertainties of the results would be smaller than one percent, and the corresponding error bars are less than the size of symbols in the plots.

Backscattered and Transmitted Fractions

Backscattering is the result of a delicate interplay of elastic scattering and energy-loss events. A few global features (e.g., the variation of the η_B with the energy E_0 of the incident beam, or with the thickness of the specimen) can be understood in terms of integrals of the DCSs, the most relevant being the transport mean free path (Salvat *et al.*, 2005) and the inelastic mean free path, Eq. (20). Detailed information obtained from experimental measurements, such as angular and energy distributions of backscattered electrons, can only be reproduced by simulations implementing realistic DCS models.

Figure 1 displays backscattering coefficients, η_B , of electron beams impinging normally on thick specimens of Be, Al, Cu and Au, with energies from 0.1 keV to 400 keV. Simulation results are seen to be in reasonable agreement with experimental data from the database compiled by Joy (2008). Unfortunately, experimental

uncertainties are quite large, as revealed by the spread of measurement data from different authors.

For the sake of comparison, Figure 1 also displays backscattering coefficients of the four materials calculated with the program CASINO (Hovington *et al.*, '97), a well-known MC code for simulation of electron transport with a user-friendly interface. In the simulations with CASINO, the default physics model (based on tabulated elastic-scattering cross sections and experimentally determined stopping power) was selected; each simulation run involved the generation of 100,000 electron trajectories. The results from the present physics model and code seem to agree better with the experiments than those from CASINO for Be, Al, and Cu. For these materials CASINO gives backscattering coefficients that are systematically lower for energies below about 1 keV. In the case of Au, the two codes yield similar results. To compare the simulation speeds of our code and CASINO, we performed simulation runs of the two codes for Al and Au, with electron beam energies of 10 keV and 30 keV, and 1 million incident electrons in each run. In the case of Al, CASINO took 680 and 1717 seconds for the 10 keV and the 30 keV cases, respectively. The corresponding execution times of our code were similar, 687 and 1771 seconds. In the case of Au,

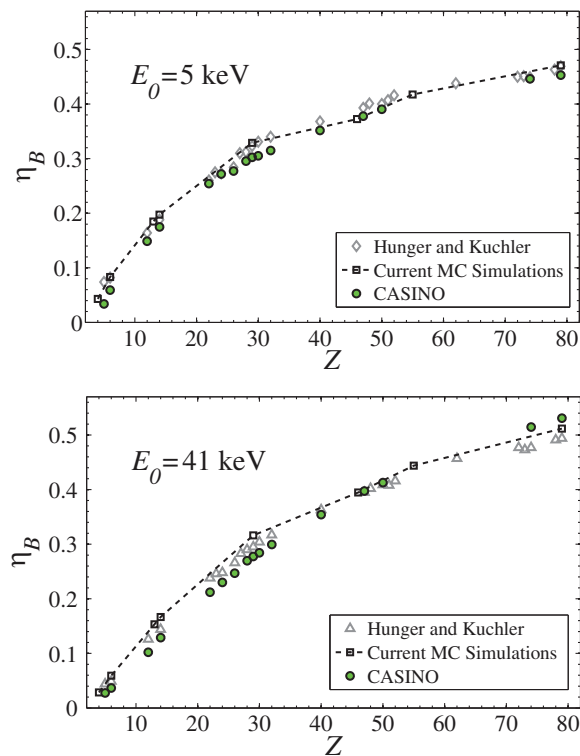


Fig 2. Variation of the backscattering coefficient with the atomic number for electron beams with initial energies of $E_0 = 5$ and 41 keV impinging normally on elemental samples. The lines are results from present simulations. Open diamonds and triangles represent experimental data from Hunger and Kuchler (1979). Circles are simulation results from the program CASINO.

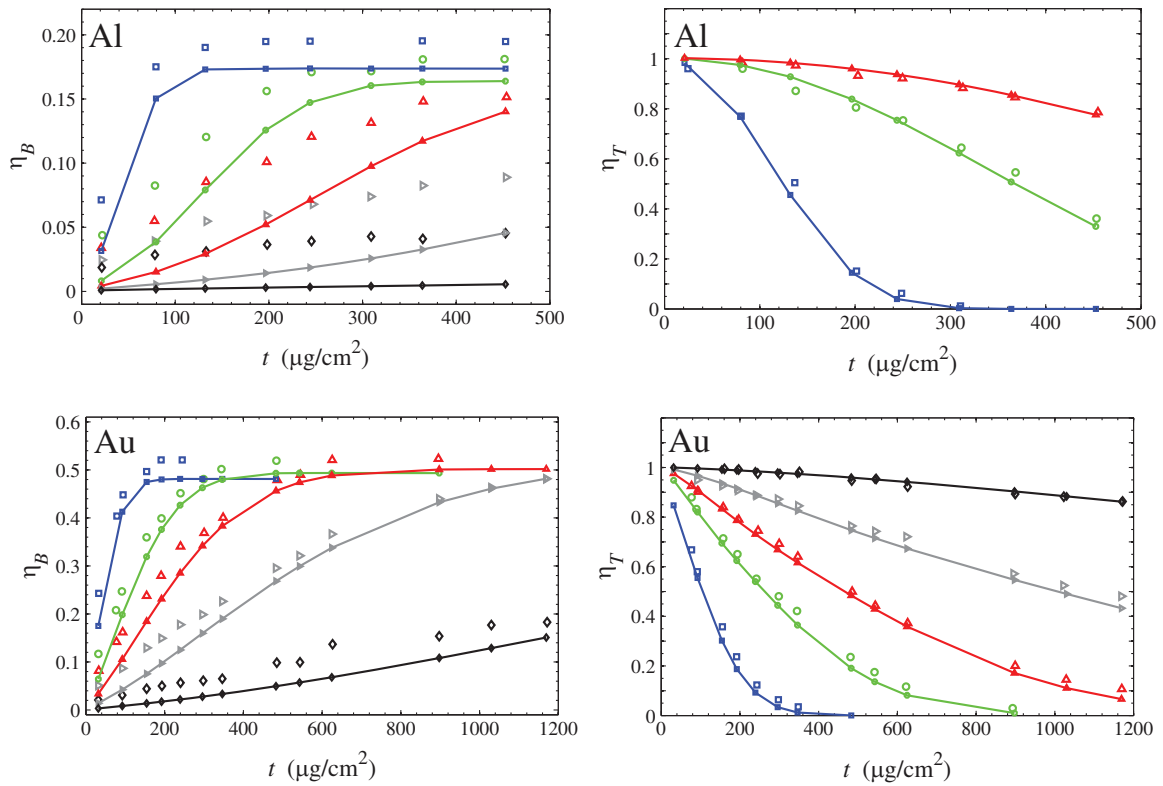


Fig 3. Backscattering and transmission coefficients, η_B and η_T of electron beams with energy E_0 impinging normally on Al and Au thin films, as functions of the film thickness. Lines are results from present simulations. Symbols represent the experimental data from Reimer and Drescher ('77). \square , $E_0 = 9.3$ keV; \circ , $E_0 = 17.3$ keV; \triangle , $E_0 = 25.2$ keV; \triangleright , $E_0 = 41.5$ keV; \diamond , $E_0 = 102$ keV.

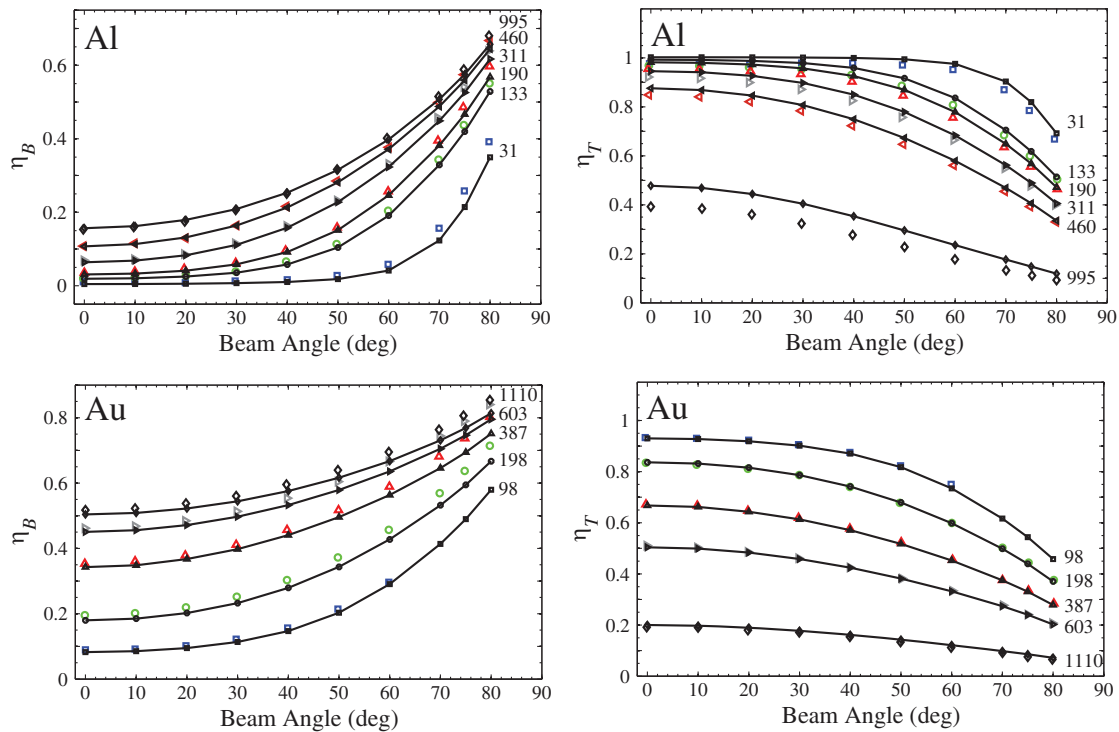


Fig 4. Backscattering and transmission coefficients of 30-keV electron beams impinging on thin Al and Au films as functions of the angle of incidence. Solid lines are results from the present simulations, symbols represent experimental data from Neubert and Rogaschewski ('84). The numerals at the end of each dataset indicates the film thickness in $\mu\text{g}/\text{cm}^2$.

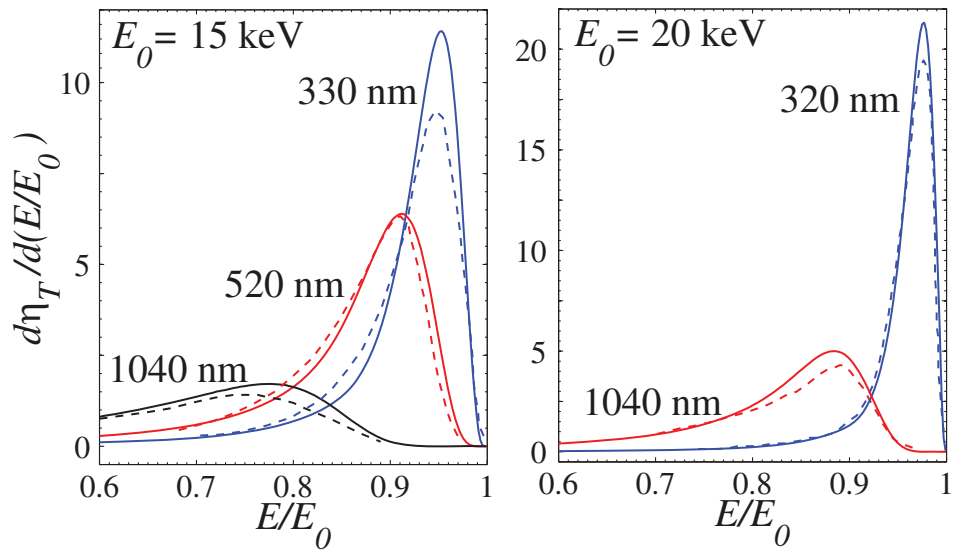


Fig 5. Energy distributions of electrons from beams with initial energies of $E_0 = 15$ and 20 keV at normal incidence transmitted through Al films of various thicknesses. Continuous lines are results from our MC simulations and dashed lines represent experimental data from Refs. (Shimizu et al., '75, '76).

our code completed the 10 keV and the 30 keV runs in 268 and 814 seconds, respectively. The corresponding runs with CASINO took 469 and 1895 seconds, respectively.

Figure 2 illustrates the dependence of the backscattering coefficient on the atomic number Z of the specimen, for electron beams of 5 keV and 41 keV at normal incidence. Simulation results are seen to be in close agreement with experimental measurements by Hunger and Kuchler (Hunger and Kuchler, '79) and with the results from simulations with the CASINO program. The increase of the backscattering coefficient with Z

results from the prevalence of elastic scattering against inelastic interactions.

Backscattering and transmission coefficients of electron beams of various energies impinging normally on thin films of Al and Au are displayed in Figure 3 as functions of the film thickness. Results from our simulations are compared with data measured by Reimer and Drescher (Reimer and Drescher, '77). Agreement between simulated and measured transmission coefficients is satisfactory. However, simulated backscattering coefficients are systematically lower than measurements. This difference is partially due to

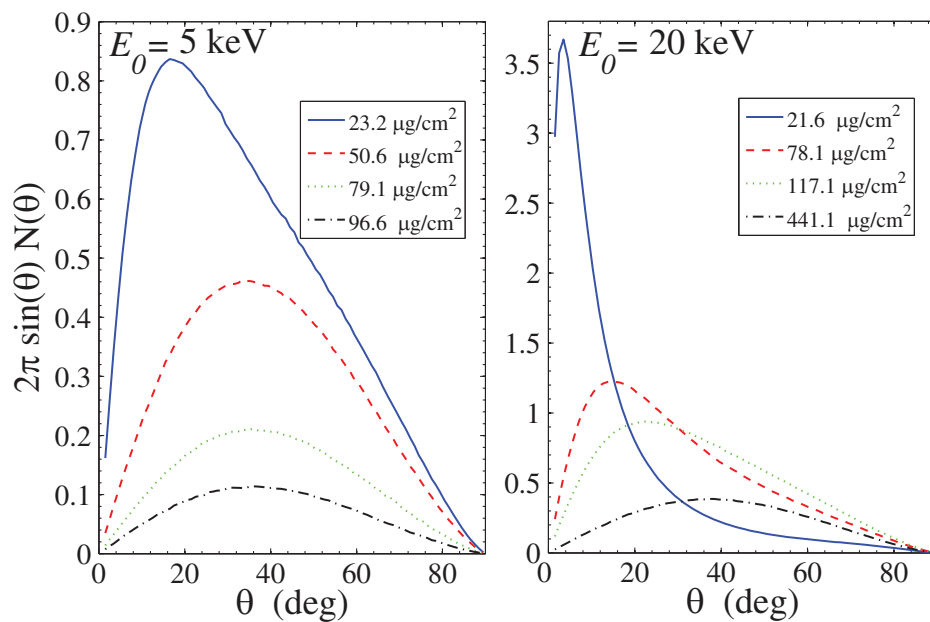


Fig 6. Simulated angular distribution of electrons transmitted through Au films of the indicated thicknesses, for beams with initial energies of 5 and 20 keV and normal incidence.

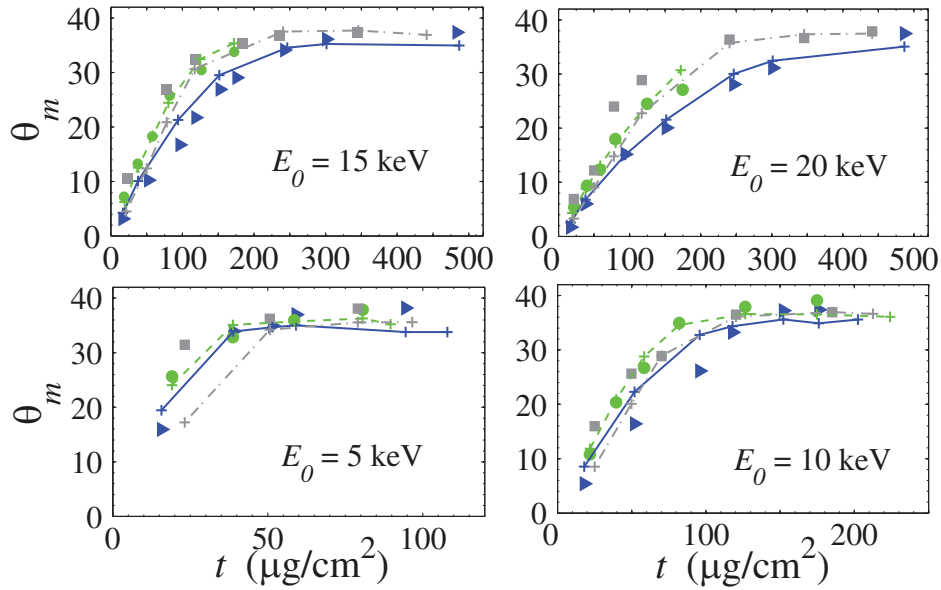


Fig 7. Most probable deflection angle θ_m of electrons energies transmitted through films of Al (\blacktriangleright), Cu (\circ) and Au (\square), for different beam energies, as a function of the film thickness t . The lines are results from the present simulations (solid, dash and dash-dot lines are for Al, Cu and Au, respectively); symbols represent experimental data from Cosslett and Thomas ('64).

the retarding electric fields in the experimental arrangement, which cause low-energy transmitted electrons to be deflected back and cross the film.

Figure 4 shows the variation of the backscattering and transmission coefficients with the angle of incidence of 30-keV-electron beams in thin films of Al and Au. Our simulation results agree closely with experimental measurements by Neubert and Rogaschewski ('84).

Energy and Angular Distributions

Let us now analyze the energy and angular distributions of transmitted electrons. In Figure 5 we compare energy distributions of electrons, with initial energies $E_0=15$ keV and 20 keV and at normal incidence, transmitted through Al films of various thicknesses. Our simulation results are seen to be in reasonable agreement with measurements in Refs. (Shimizu *et al.*, '75, '76). Because of the increase in the number of inelastic events, when the film thickness increases the probability of high energy transmitted electrons decreases and the maximum value of $d\eta_T/d(E/E_0)$ shifts towards lower values of E/E_0 .

Figure 6 shows simulated angular distributions $2\pi\sin(\theta)N(\theta)$ (i.e., probability per unit deflection angle) for electrons transmitted through Au thin films from beams of 5 and 20 keV at normal incidence. When film thickness increases, the most probable angle increases and the distribution becomes more symmetrical. This trend is in agreement with measurements by Cosslett and Thomas ('64). Figure 7 shows a comparison of the most probable deflection angles, θ_m , for electrons transmitted through thin films of Al, Cu and Au obtained

from our simulations with experimental data of Cosslett and Thomas ('64). The saturation value of θ_m is seen to be quite independent of the atomic number.

The depth-dose distribution (i.e., deposited energy per unit depth and per incident electron) results from the combined effect of elastic scattering and energy loss. It therefore represents a demanding test to the interaction models adopted in simulation. Figure 8 compares normalized depth-dose distributions measured by Werner *et al.* ('88) for electrons of various energies in Si, at normal incidence, with results from our simulations. The agreement between our MC simulation results and the experimental measurements is again satisfactory.

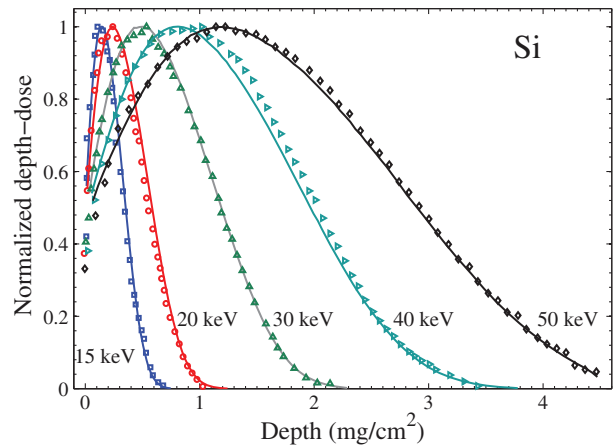


Fig 8. Depth-dose distribution of electron beams at normal incidence and with the indicated energies in Si. Continuous lines represent results from the present simulations. Symbols are experimental data from Werner *et al.* ('88).

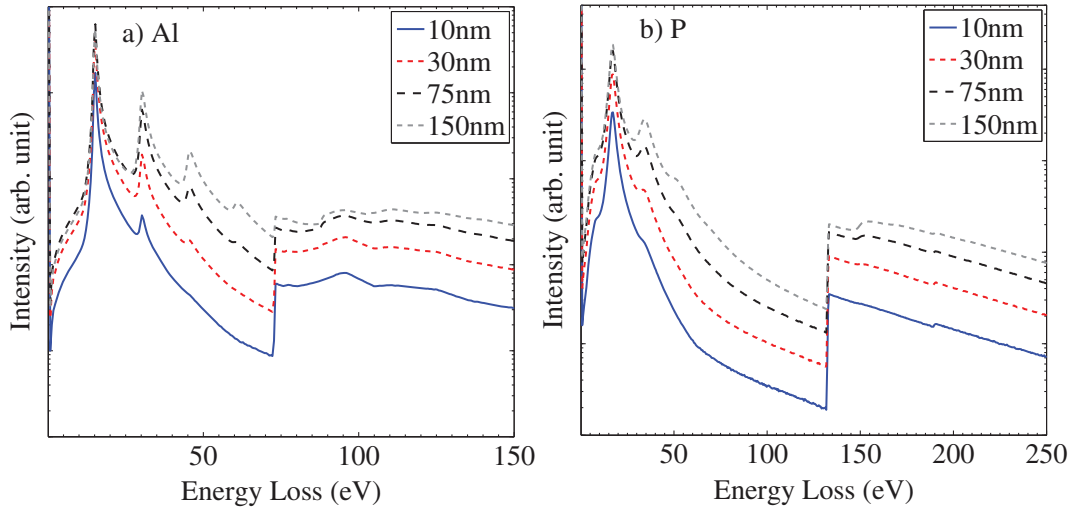


Fig 9. Simulated EEL spectra for 200-keV electrons in (a) Al and (b) P films of the indicated thicknesses. The scale of the vertical axis is logarithmic.

Electron Energy-Loss Spectra

We now turn to the simulation of electron energy-loss (EEL) spectra. Specifically, we consider a converging beam with probe-illumination angle of 2 mrad centered on the normal to the target, and we simulate the energy distribution of electrons that are transmitted with deflections less than the collection angle of the detector, which we set equal to 10 mrad. Figure 9 displays simulated EEL spectra of 200-keV electrons in Al and P films of different thicknesses. All the EEL spectra are normalized to one incident electron. The spectra clearly show the occurrence of multiple plasmon excitations, as well as ionizations of the L_3 subshell. Both the number of plasmon excitations and the intensity of the background increase with the foil thickness.

Figure 10 shows the signal (peak) to background ratio (SBR) at the L_3 ionization edge for Al and Si as well as O K and Ni L_{2-3} of NiO for various beam energies as a function of the film thickness in units of the mean free path for inelastic collisions. As the film thickness increases, the SBR decreases because spectral features at high energy losses are smoothed off by low-energy excitations, which are much more probable than high-energy excitations. The nearly exponential decrease of the SBR with t/λ_{in} is in agreement with the theoretical analysis by Leapman (Ahn, 2004).

Another quantity of interest is the signal-to-noise ratio (SNR), defined as:

$$SNR = \frac{I_E - I_B}{\sqrt{I_E}}. \quad (51)$$

where I_E and I_B are, respectively, the signal and background intensities at the ionization edge. This definition follows from the formula proposed by Egerton ('82), $SNR = I_k / [I_k + I_b + \text{var}(I_b)]^{1/2}$, where

I_k and I_b represent, respectively, the signal and background areas over a selected interval of energy losses. In our case, these areas are proportional to $I_E - I_B$ and I_B , respectively, and we can set $\text{var}(I_B) = 0$, because the background intensity (at the edge energy) is well defined.

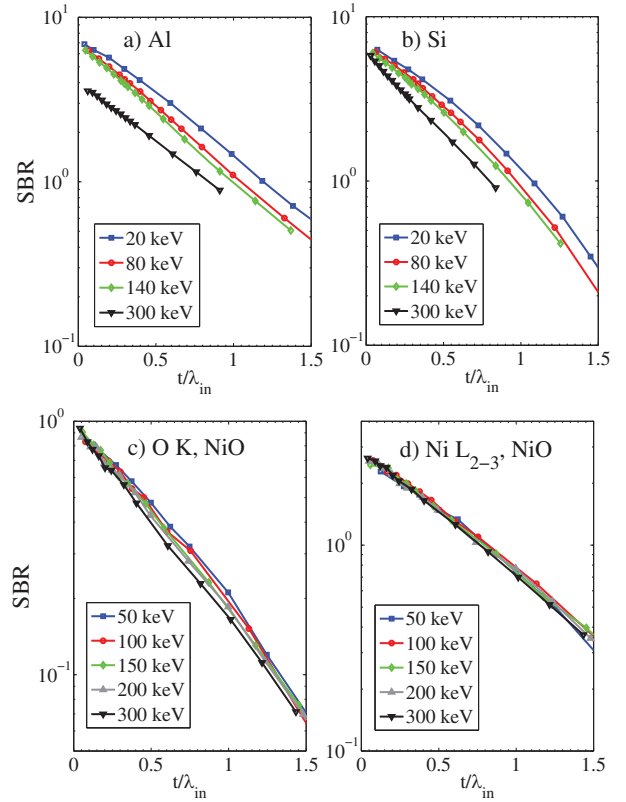


Fig 10. Simulated signal-to-background ratio (SBR) of the L_3 edge of Al (a) and Si (b) in single-element specimens, and of the K edge of O (c) and the L_{2-3} edges of Ni (d) in NiO, at different beam energies as a function of film thickness.

Figure 11 shows the SNR at the L_3 edge of Al and Si as well as O K and Ni L_{2-3} of NiO for various beam energies as a function of film thickness. The SNR and SBR for O K and Ni L_{2-3} edges in NiO follow the same trend as the L_3 edges for Al and Si. The SNR-vs.-thickness curves present a broad maximum, corresponding to the optimal thickness t_m for recording the EEL spectrum. For thicker films, the background intensity increases, and the edge signal becomes weaker (Egerton, 2011).

The results in Figure 11 indicate that the reduced optimum thickness, t_m/λ_{in} , stays essentially constant with the beam energy. This implies that, given the optimum thickness $t_m(E_1)$ at a certain energy E_1 , the simple formula

$$t_m(E) \simeq t_m(E_1) \frac{\lambda_{in}(E)}{\lambda_{in}(E_1)}, \quad (52)$$

can be used to estimate the optimum thickness for any other energy. The values from this formula do not differ much the approximation suggested by Leapman (Ahn, 2004),

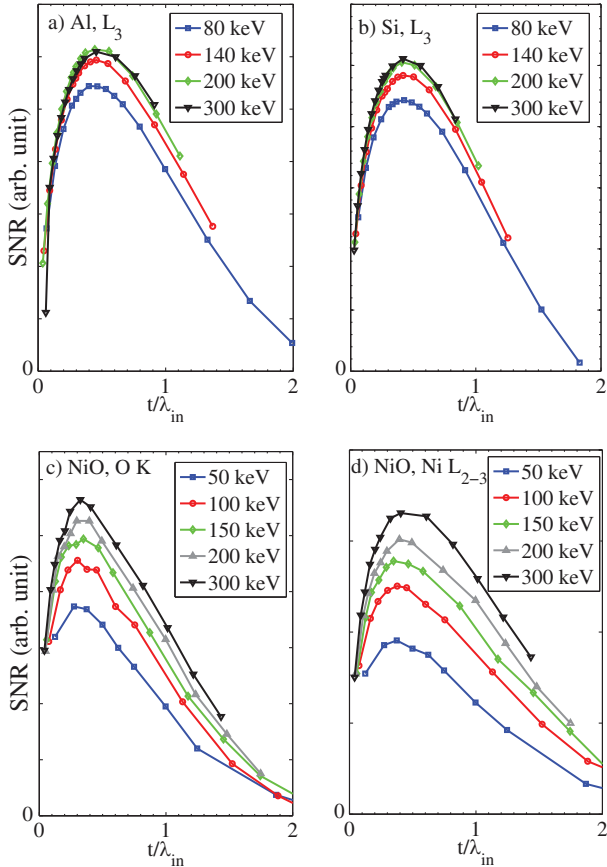


Fig 11. Simulated signal-to-noise ratio (SNR) of the L_3 edge for (a) Al, (b) Si, (c) O K and (d) Ni L_{2-3} of NiO at different beam energies as a function of film thickness.

$$t_m = \frac{\lambda_{in}\lambda_e}{2\lambda_{in} + \lambda_e}, \quad (53)$$

Figure 12 shows the t_m values predicted by this formula, with the mean free paths corresponding to the interaction models used in the simulations, for Al and Si and energies between 50 keV and 300 keV. Indeed, the values so obtained are close to those inferred from simulation (see Fig. 11). It should be mentioned that Eq. (53) is an approximation and it gives a t_m which does not depend on the amount of energy loss.

Finally, Figure 13 displays the results from simulations of EEL spectra of 200-keV electrons in NiO and the corresponding SBRs for the O K edge and Ni L edge, for various film thicknesses. The probe illumination and collection angles used in the simulations were 9 and 18 mrad, respectively. Calculated SBRs are in close agreement with values derived (from spectral areas) from measurements by Huber *et al.* (2010).

Concluding Remarks

We have presented a generic MC algorithm for detailed simulation of electron transport in bulk specimens and foils. The adopted interaction models can be adapted to describe electron transport in arbitrary materials. The DCSs for elastic scattering were calculated using the relativistic partial-wave code ELSEPA (Salvat *et al.*, 2005), which allows considering different scattering potentials. The OOS, which completely determines the DCS for inelastic collision, can be assembled by combining atomic photoabsorption cross sections with low-energy optical oscillator strengths obtained either from experimental optical data or from density functional theory calculations. Comparison of simulation results with a variety of experimental measurements shows that our MC code provides a realistic description of the penetration and energy loss of electrons in solids, within the considered

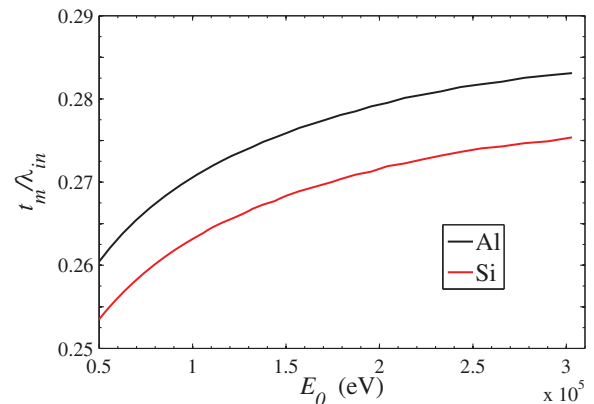


Fig 12. Optimum thickness as a function of the beam energy, calculated from the Leapman formula, Eq. (53), for Al and Si.

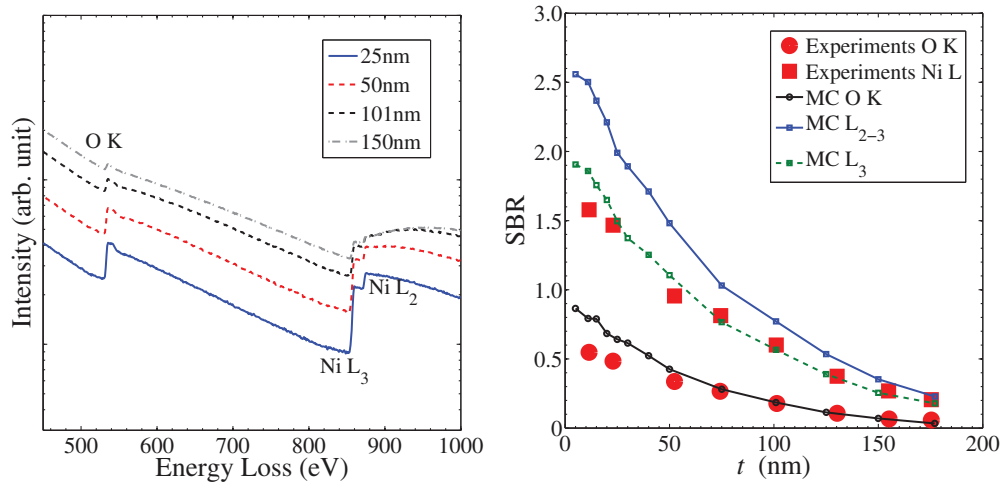


Fig 13. Simulated EEL spectra of NiO from films with the indicated thicknesses, and SBRs for the O K and Ni L edges as functions of the film thickness t . Experimental data are from Huber et al. (2010). The scale of the vertical axis for simulated EEL spectra of NiO is logarithmic.

energy range. As an application, we have considered the practical use of the code in EEL spectroscopy.

Acknowledgments

The National Sciences and Engineering Research Council of Canada (NSERC) and the McGill Engineering Doctoral Awards (MEDA) program are acknowledged for financial support. Also, financial support from the Spanish Ministerio de Ciencia e Innovación and FEDER (project no. FPA2009-14091-C02) and from the Generalitat de Catalunya (grant SGR 2009-276) is gratefully acknowledged.

References

- Ahn CC. 2004. Transmission Electron Energy Loss Spectrometry in Materials Science and The EELS Atlas. 2nd Edition. Germany: Wiley-VCH Verlag GmbH and Co. KGaA.
- Ambrosch-Draxl C, Sofo JO. 2006. Linear optical properties of solids within the full-potential linearized augmented plane wave method. *Comp Phys Comm* 175:1–14.
- Becke AD, Johnson ER. 2006. A simple effective potential for exchange. *J Chem Phys* 124:221101.
- Berger MJ, Hubbell JH, Seltzer SM, Chang J, Coursey JS, Sukumar R, Zucker DS. 2005. XCOM: Photon Cross Sections Database. Tech. rep., Institute of Standards and Technology, Gaithersburg, MD, available from <http://physics.nist.gov/PhysRefData/Xcom/Text/XCOM.html>
- Blaha P, Schwarz K, Madsen G, Kvasnicka D, Luitz J. 2001. WIEN2K: An Augmented Plane Wave Plus Local Orbitals Program for Calculating Crystal Properties. Technical University of Vienna, Vienna.
- Bote D, Salvat F. 2008. Calculations of inner-shell ionization by electron impact with the distorted-wave and plane-wave Born approximations. *Phys Rev A* 77:042701.
- Bote D, Salvat F, Jablonski A, Powell CJ. 2009. The effect of inelastic absorption on the elastic scattering of electrons and positrons in amorphous solids. *J Electron Spectrosc Rel Phenom* 175:41–54.
- Cosslett VE, Thomas RN. 1964. Multiple scattering of 5-30 keV electrons in evaporated metal films: I. Total transmission and angular distribution. *Brit J Appl Phys*. 15:883–907.
- Cullen DE, Hubbell JH, Kissel L. 1997. EPDL97 The Evaluated Data Library, 97 Version, Tech. Rep. UCRL-50400, Lawrence Livermore National Laboratory, Livermore, California.
- Egerton RF. 1982. A revised expression for signal/noise ratio in EELS. *Ultramicroscopy* 9:387–390.
- Egerton RF. 2011. Electron Energy-Loss Spectroscopy in the Electron Microscope. 3rd ed. New York: Springer.
- Fano U. 1963. Penetration of protons, alpha particles and mesons. *Ann Rev Nucl Sci* 13:1–66.
- Fernández-Varea JM, Mayol R, Liljequist D, Salvat F. 1993. Inelastic scattering of electrons in solids from a generalized oscillator strength model using optical and photoelectric data. *J Phys Condens Matter* 5:3593–3610.
- Fernández-Varea JM, Liljequist D, Csillag S, Rätty R, Salvat F. 1996. Monte Carlo simulation of 0.1-100 keV electron and positron transport in solids using optical data and partial wave methods. *Nucl Instrum Meth B* 108:35–50.
- Fernández-Varea JM, Salvat F, Dingfelder M, Liljequist D. 2005. A relativistic optical-data model for inelastic scattering of electrons and positrons in condensed matter. *Nucl Instrum Meth B* 229:187–218.
- Furness JB, McCarthy IE. 1973. Semiphenomenological optical model for electron scattering on atoms. *J Phys B Atom Mol Phys* 6:2280–2291.
- Gauvin R, Lifshin E, Demers H, Horny P, Campbell H. 2006. Win X-ray: a new Monte Carlo program that computes X-ray spectra obtained with a scanning electron microscope. *Microsc Microanal* 12:49–64.
- Hovington P, Drouinm D, Gauvin R. 1997. CASINO: A New Monte Carlo Code in C Language for Electron Beam Interaction - Part I: Description of the Program. *Scanning* 19:1–14. The software is available at <http://www.gel.usherbrooke.ca/casino/>
- Huber D, Fraser HL, Klenov DO, Harrach HS, Zaluzec NJ. 2010. Relative Sensitivity of XEDS vs EELS in the AEM. Late Breaking Poster, Microscopy and Microanalysis Portland.
- Hunger HJ, Kuchler L. 1979. Measurements of the electron backscattering coefficient for quantitative EPMA in the energy range of 4 to 40 keV. *Phys Status Solidi (A)* 56: K45–K48.
- ICRU Report 77. 2007. Elastic Scattering of Electrons and Positrons. (Bethesda, MD).

- Inokuti M. 1971. Inelastic collisions of fast charged particles with atoms and molecules—The Bethe theory revisited. *Rev Mod Phys* 43:297–347.
- Jensen KO, Walker AB. 1993. Monte Carlo simulation of the transport of fast electrons and positrons in solids. *Surf Sci* 292:83–97.
- Joy DC. 1995. *Monte Carlo Modeling for Electron Microscopy and Microanalysis*. New York: Oxford University press.
- Joy DC. 2008. A Database of electron solid interactions Revision 08-1. E.M. Facility, University of Tennessee, and Oak Ridge National Laboratory, Knoxville, available from <http://web.utk.edu/~srcutk/htm/interact.htm>
- Koller D, Tran F, Blaha P. 2011. Merits and limits of the modified Becke-Johnson exchange potential. *Phys Rev B* 83:195134.
- Lindhard J. 1954. On the properties of a gas of charged particles. *Dan Mat Fys Medd* 28:1–57.
- Moller C. 1932. Zur Theorie des Durchgangs schneller Elektronen durch Materie. *Ann Physik* 14:531–585.
- Neubert G, Rogaschewski S. 1984. Measurements of the back-scattering and absorption of 15-60 keV electrons for transparent solid films at various angles of incidence. *J Phys D: Appl Phys* 17:2439–2454.
- Ochkur VI. 1965. Ionization of the hydrogen atom by electron impact with allowance for the exchange. *Sov Phys JETP* 20:1175–1178.
- Palik ED (Ed.). 1985. *Handbook of Optical Constants of Solids*. San Diego, CA: Academic Press.
- Palik ED (Ed.). 1991. *Handbook of Optical Constants of Solids II*. San Diego, CA: Academic Press.
- Palik ED (Ed.). 1998. *Handbook of Optical Constants of Solids III*. San Diego, CA: Academic Press.
- Perdew JP, Burke K, Ernzerhof M. 1996. Generalized gradient approximation made simple. *Phys Rev Lett* 77:3865.
- Reimer L, Drescher H. 1977. Secondary electron emission of 10-100 keV electrons from transparent films of Al and Au. *J Phys D: Appl Phys* 10:805–815.
- Salvat F. 2003. Optical-model potential for electron and positron elastic scattering by atoms. *Phys Rev A* 68:012708.
- Salvat F, Jablonski A, Powell CJ. 2005. ELSEPA-Dirac partial-wave calculation of elastic scattering of electrons and positrons by atoms, positive ions and molecules. *Comput Phys Commun* 165:157–190.
- Salvat F, Fernández-Varea JM, Sempau J. 2011. sc penelope-2011: A code System for Monte Carlo Simulation of Electron and Photon Transport, OECD/NEA Data Bank, Issy-les-Moulineaux, France, available from <http://www.nea.fr/lists/penelope.html>
- Schwarz K, Blaha P. 2003. Solid state calculations using WIEN2k. *Comput Mater Sci* 28:259–273.
- Scofield JH. 1973. Theoretical photoionization cross sections from 1 to 1500 keV. Tech. Rep. UCRL-51326, Lawrence Livermore Laboratory, Livermore, California.
- Shimizu R, Kataoka Y, Matsukawa T, Ikuta T, Murata K, Hashimoto H. 1975. Energy distribution measurements of transmitted electrons and Monte Carlo simulation for kilovolt electron. *J Phys D: Appl Phys* 8:820–828.
- Shimizu R, Kataoka Y, Ikuta T, Koshikawat T, Hashimoto H. 1976. A Monte Carlo approach to the direct simulation of electron penetration in solids. *J Phys D: Appl Phys* 9:101–114.
- Shimizu R, Ding ZJ. 1992. Monte Carlo modelling of electron-solid interactions. *Rep Prog Phys* 55:487–531.
- Werner U, Koch F, Oelgart G. 1988. Kilovolt electron energy loss distribution in Si. *J Phys D: Appl Phys* 21:116–124.
- Werner WSM, Glantschnig K, Ambrosch-Draxl C. 2009. Optical constants and inelastic electron-scattering data for 17 elemental metals. *J Phys Chem Ref Data* 38:1013–1092.